MIT Open Access Articles

An Eddy-Permitting Southern Ocean State Estimate

The MIT Faculty has made this article openly available. ***Please share*** how this access benefits you. Your story matters.

Citation	Mazloff, Matthew R, Patrick Heimbach, and Carl Wunsch. "An Eddy-Permitting Southern Ocean State Estimate." Journal of Physical Oceanography 40.5 (2010) : 880-899. c2010 American Meteorological Society
As Published	http://dx.doi.org/10.1175/2009jpo4236.1
Publisher	American Meteorological Society
Version	Final published version
Citable link	http://hdl.handle.net/1721.1/62590
Terms of Use	Article is made available in accordance with the publisher's policy and may be subject to US copyright law. Please refer to the publisher's site for terms of use.

Massachusetts Institute of Technology

DSpace@MIT

An Eddy-Permitting Southern Ocean State Estimate

MATTHEW R. MAZLOFF

Scripps Institution of Oceanography, La Jolla, California

PATRICK HEIMBACH AND CARL WUNSCH

Massachusetts Institute of Technology, Cambridge, Massachusetts

(Manuscript received 6 February 2009, in final form 14 December 2009)

ABSTRACT

An eddy-permitting general circulation model of the Southern Ocean is fit by constrained least squares to a large observational dataset during 2005–06. Data used include Argo float profiles, CTD synoptic sections, Southern Elephant Seals as Oceanographic Samplers (SEaOS) instrument-mounted seal profiles, XBTs, altimetric observations [*Envisat*, *Geosat*, *Jason-1*, and Ocean Topography Experiment (TOPEX)/Poseidon], and infrared and microwave radiometer observed sea surface temperature. An adjoint model is used to determine descent directions in minimizing a misfit function, each of whose elements has been weighted by an estimate of the observational plus model error. The model is brought into near agreement with the data by adjusting its control vector, here consisting of initial and meteorological boundary conditions. Although total consistency has not yet been achieved, the existing solution is in good agreement with the great majority of the 2005 and 2006 Southern Ocean observations and better represents these data than does the *World Ocean Atlas 2001* (*WOA01*) climatological product. The estimate captures the oceanic temporal variability and in this respect represents a major improvement upon earlier static inverse estimates. During the estimation period, the Drake Passage volume transport is 153 ± 5 Sv (1 Sv ≡ 10^6 m^3 s^{-1}). The Ross and Weddell polar gyre transports are 20 ± 5 Sv and 40 ± 8 Sv, respectively. Across 32°S there is a surface meridional overturning cell of 12 ± 12 Sv, an intermediate cell of 17 ± 12 Sv, and an abyssal cell of 13 ± 6 Sv. The northward heat and freshwater anomaly transports across 30°S are −0.3 PW and 0.7 Sv, with estimated uncertainties of 0.5 PW and 0.2 Sv. The net rate of wind work is 2.1 ± 1.1 TW. Southern Ocean theories involving short temporal- and spatial-scale dynamics may now be tested with a dynamically and thermodynamically realistic general circulation model solution that is known to be compatible with the modern observational datasets.

1. Introduction

The Southern Ocean circulation is dynamically distinct from all other ocean regions in that it is characterized by a strong circumpolar current (Crease 1964). The region also has a known strong temporal variability (Gille and Kelly 1996; Wunsch and Heimbach 2009). Its remoteness and distinctiveness have greatly inhibited both observations and dynamical understanding of the controls on its circulation and corresponding properties such as freshwater transports. Various reviews (Rintoul et al. 2001; Olbers et al. 2004) concur that geostrophic eddy activity plays a large role in the local dynamics (e.g., in the vorticity budget, Hughes 2005). The presence of a strong eddy field produces great difficulties for observing large-scale and low-frequency phenomena. Eddy dynamics are most prominent near the first baroclinic Rossby deformation radius, which ranges from ~30 km at 40°S to less than 10 km near Antarctica (Chelton et al. 1998); resolving these scales, both in models and with observations, is a formidable challenge. Unlike mid- and low-latitude oceans, sea ice behavior must also be directly accounted for.

Historical Southern Ocean observations are extremely sparse, such that one must be wary of circulation estimates made before the start of large-scale measurement efforts. These efforts began in earnest with the *Eltanin* cruises in the early 1960s (Gordon and Molinelli 1982). Although becoming more frequent after 1962, observational efforts

Corresponding author address: Matthew Mazloff, Scripps Institution of Oceanography, UCSD, 9500 Gilman Drive, La Jolla, CA 92093-0230.
E-mail: mmazloff@ucsd.edu

DOI: 10.1175/2009JPO4236.1

© 2010 American Meteorological Society

were focused in specific regions such as the Drake Passage. Coverage significantly improved in both space and time with the introduction of the Ocean Topography Experiment (TOPEX)/Poseidon (T/P) high-precision satellite altimeter in 1992 and further in 2002 with the introduction of hundreds of autonomous floats through the Argo program (Gould et al. 2004). In 2003 the Southern Elephant Seals as Oceanographic Samplers (SEaOS) program (available online at http://biology.st-andrews.ac.uk/seaos) began mounting CTD instruments and GPS navigators on elephant seals to gather data in the polar regions (Boehme et al. 2008). For the first time, Southern Ocean observations are relatively abundant, to the point that constraining an ocean circulation model with these data can plausibly produce an estimate of the Southern Ocean state significantly better than one produced from the data or model alone.

To date, most inverse model estimates of the Southern Ocean state have been ''static'' and thus are to be interpreted as either snapshots or as some vaguely defined climatological average (e.g., Ganachaud and Wunsch 2003). Besides lacking temporal resolution, these estimates have primarily employed hydrographic sections separated spatially by distances far larger than any eddy scale. The few existing nonstatic ocean state estimates made by synthesizing observations and general circulation models have only been made at spatial resolutions and temporal separations far too coarse to resolve the sharp fronts and energetic eddies in the region (Stammer et al. 2002; Wunsch and Heimbach 2007).

Unconstrained general circulation models (GCMs) of the Southern Ocean have been constructed that are beginning to resolve eddy dynamics. Much of what is known about the Southern Ocean dynamics comes from these models [e.g., Killworth (1992), Saunders and Thompson (1993), and Döös and Webb (1994) with the Fine Resolution Antarctic Model (FRAM) and Lee and Coward (2003) with the Ocean Circulation and Climate Advanced Modeling (OCCAM) model]. However, these models have shortcomings, one being that the surface is often relaxed to climatological values. Also, they often lack mixed layer and other parameterizations (Hughes et al. 1999; Killworth et al. 2000; Treguier et al. 2007) and so are not entirely physically realistic. Furthermore, the absence of full quantitative tests against the data makes inferences from these GCMs difficult to evaluate. It is known that these models have significant biases in temperature and salinity with respect to observations, translating to significant errors in transport calculations (Killworth and Nanneh 1994; Killworth et al. 2000; Olbers et al. 2004).

Despite their limitations, the GCMs do capture much of the physics believed dominant in the Southern Ocean. The hypothesis here is that, by appropriately combining one of these models with the modern datasets, a skillful and useful estimate of the time-evolving state of the Southern Ocean can be made available.

A central purpose of this work is to demonstrate the adequacy and usefulness of this Southern Ocean state estimate (SOSE) and to provide a basic quantitative description of the circulation and its variability in the early twenty-first century. Such an estimate has several important uses: 1) providing a quantitatively useful baseline for detecting past and future climate shifts and 2) as a basis for analyzing the underlying physics controlling the circulation so as to understand if and how it might differ in other climates. The primary focus here is the first of these goals, a quantitative description of the recent circulation, which lays the foundation for a discussion (Mazloff 2008; M. R. Mazloff and R. Ferrari 2010, unpublished manuscript) directed explicitly at the second goal: the physics of the circumpolar region.

2. A model–observation least squares optimization

A regional eddy-permitting Southern Ocean state estimate has been constructed using the machinery developed by the consortium for Estimating the Circulation and Climate of the Ocean (ECCO; see online at http://www.ecco-group.org). The basic ECCO Global Ocean Data Assimilation Experiment (ECCO-GODAE) approach, as described by Wunsch and Heimbach (2007), involves obtaining a least squares fit of an oceanic GCM to the great majority of meteorological and oceanic observations, of all types, over a finite time interval. The goal is a three-dimensional time-evolving exact solution to the known equations of the GCM that are simultaneously consistent, as far as practical, with the observations. The central ECCO-GODAE effort has been directed toward obtaining a global solution. Here, in the interests of increasing spatial resolution to that required for realism at high latitudes (Fig. 1), the region of interest is restricted to the Southern Ocean poleward of 25°S. The estimation interval is limited to 2005–06, the beginning of which marks the start of major Southern Ocean Argo float deployment and takes advantage of the ongoing altimetric measurements as well as numerous other datasets (Table 1) described more completely in Mazloff (2008).

The SOSE model is an evolved version of the Massachusetts Institute of Technology GCM (MITgcm) (Marshall et al. 1997), having 1/6° horizontal resolution, 42 vertical levels of varying thickness, and a 900-s time step. Because the resolution remains finite, parameterizations are still required and are the same as used in Forget (2010), a difference being that the mixing coefficients are smaller, reflecting the higher resolution.

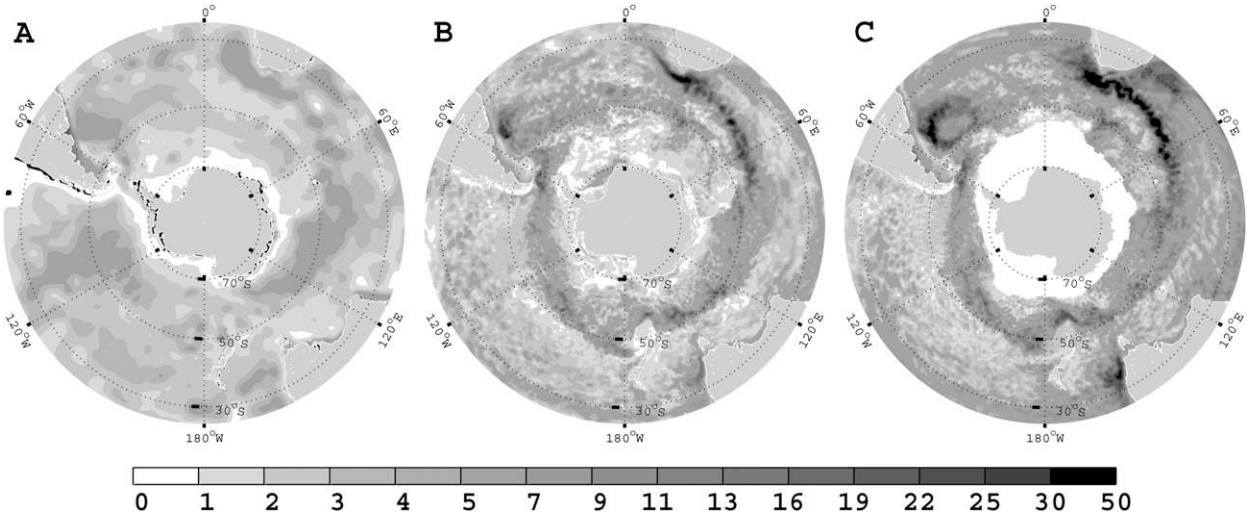

FIG. 1. Standard deviation of SSH (cm) for (a) a 1° state estimate (Forget 2010), (b) the 1/6° SOSE, and (c) an optimally interpolated (OI) satellite altimetry product (available online at http://www.aviso.oceanobs.com). There is limited satellite altimetry information close to Antarctica because of the presence of sea ice. The color axis is nonlinear. SSH variance arises largely from wind-driven barotropic waves and from ocean circulation instabilities that give rise to eddies and meanders. While both these processes are active in the higher-resolution SOSE, it is mainly the barotropic fluctuations that are responsible for the SSH variance in the coarser 1° resolution state estimate. Increased resolution is vital to reproducing the observed variance of the Southern Ocean.

These coefficients (Table 2) are typical of those used in other eddy-permitting models (e.g., Saunders and Thompson 1993; Gebbie et al. 2006). A sea ice thermodynamical model, based on the work of Hibler (1980), is employed (Losch et al. 2010). See Mazloff (2008) for additional details.

Model ability to reproduce the data is measured with a ''cost'' or '' misfit'' or ''objective'' function $\mathcal{J}$, which is the scalar sum over time and space of weighted squared model state and data differences. The weights are prescribed in the form of a reciprocal error variance. As in any least squares solution, the prescribed uncertainty dictates the extent to which the model is required to reproduce any particular observation; thus, the weights have a strong influence on the solution obtained. The weights used for the SOSE are identical to those used in

TABLE 1. Constraining datasets used in the SOSE. Each and every constraint is given a weight; thus, the number of constraints shown in the third column does not necessarily represent the dataset's influence in the estimate. See Mazloff (2008) for a discussion of the constraints and their implementation. The state estimate of Forget (2010) is used to constrain the initial conditions.

Instrument	Observation	Number in 2005–06 SOSE	Source
Argo	Salinity	2 072 885	Coriolis Argo Data Center
CTD	Salinity	30 731	WOCE
SEaOS	Salinity	162 993	SEaOS program
Argo	Temperature	2 132 968	Coriolis Argo Data Center
CTD	Temperature	30 793	WOCE
SEaOS	Temperature	212 661	SEaOS program
XBT	Temperature	47 097	D. Berhinger, NCEP (2005)
Infrared radiometer	Surface temperature	5 620 907	Reynolds et al. (2002), NOAA
Microwave radiometer	Surface temperature	4 730 684	Remote sensing system
Merged T/P and *Jason-1*	SLA	7 323 456	Physical Oceanography Distributed Active Archive Center (PODAAC)
Envisat	SLA	3 881 190	AVISO
GFO	SLA	3 361 985	U.S. Navy, NOAA
EIGEN-GRACE-03S geoid model	Mean ocean height	524 986	(Reigber et al. 2005)
Climatology	Salinity	~2 000 000	*WOA01* (Conkright et al. 2002)
Near surface	Temperature	~2 000 000	
Climatology	Salinity	~200 000	Gouretski and Koltermann (2004)
Below 300 m	Temperature	~200 000	
Near-surface atmospheric state	Various	~350 000 000	Kalnay et al. (1996), NCEP

TABLE 2. List of model parameters.

Advection scheme	Third-order direct space time
Isopycnal diffusivity	10 $m^2 s^{-1}$
Vertical diffusivity	10^{-5} $m^2 s^{-1}$
Biharmonic horizontal diffusivity	10^{10} $m^4 s^{-1}$
Vertical viscosity	10^{-4} $m^2 s^{-1}$
Horizontal viscosity	10 $m^2 s^{-1}$
Biharmonic horizontal viscosity	10^{10} $m^4 s^{-1}$
Linear bottom drag	10^{-3} m s^{-1}

the ECCO global estimates (see Forget and Wunsch 2007; Ponte et al. 2007; Wunsch and Heimbach 2007).

Optimization is sought by iteratively reducing $\mathcal{J}$ by adjusting the "control vector" $\mathbf{u}$, which in the present configuration consists of the initial conditions and the boundary (meteorological) forcing. In the SOSE modification is required for over 700 million elements of the control vector to govern a 10 trillion term ocean state and reduce a 1.4 billion term cost function (composed of weighted model–data misfit terms and weighted control vector constraints). The methodology is that of classical Lagrange multipliers but numerically exploiting the existence of an "adjoint" model produced by automatic differentiation (Giering and Kaminski 1998). The adjoint model calculates the cost function gradients with respect to the controls, $\nabla_{\mathbf{u}}\mathcal{J}$, thereby increasing the efficiency of search (optimization) algorithms. For the optimization carried out here, the quasi-Newton search algorithm of Gilbert and Lemaréchal (1989) was used.

If an acceptable misfit can be found, the state estimate is then determined by running the free model forward in time using the adjusted control vector. In that important sense, the state estimate is obtained from an unconstrained model (in contrast, e.g., to sequential methods based on numerical weather prediction "assimilation"). In a truly optimal state, and with all Gaussian fields, residual misfits would be random white noise whose square is a χ_1^2 variable. (Le Dimet and Talagrand 1986; Wunsch and Heimbach 2007)

An optimal state estimate is a running target: the model physics are continually being improved and new data become available, as does information about the error structure. The consistency of the SOSE solution with the observations was deemed acceptable for analysis after 26 iterations of the adjoint method [see Mazloff (2008) for the time history of the iterative improvements]. This iteration 26 SOSE solution is described below.

3. The control vector

As discussed above, in the adjoint methodology the control vector represents the adjustable parameters used to bring the model into agreement with the observations. In the SOSE configuration, the control vector consists of the three-dimensional initial conditions for temperature and salinity and the time-varying two-dimensional meteorological boundary conditions (i.e., the atmospheric state). Exchanges of momentum, heat, and freshwater (salt) between the atmospheric and oceanic states are determined using "bulk formulae" (Large and Yeager 2004). The first-guess initial and northern boundary conditions come from a special 1° global state estimate made for the restricted period 2004–06 (Forget 2010), which is otherwise similar to the central ECCO-GODAE global estimates. The first-guess atmospheric state comes (at 6-hourly sampling) from the National Centers for Environmental Prediction–National Center for Atmospheric Research (NCEP–NCAR) reanalysis (Kalnay et al. 1996). No quantitative estimate is available for the accuracies of this reanalysis, so the weights used are based on the calculated standard deviations of the fields. Adjustments to the first-guess atmospheric precipitation, radiation, specific humidity, and temperature fields occur at 10-day intervals. Wind field adjustments are made at 2-day intervals.

The SOSE-estimated wind fields differ from the NCEP–NCAR fields on relatively small spatial scales, while differences in the other components are basin scale (Fig. 2). Spatial and temporal variability in the SOSE winds are greater than the NCEP–NCAR fields in the Antarctic Circumpolar Current (ACC) region; largely for this reason, the eddy kinetic energy (KE) in the SOSE is ~3% greater than the first-guess model solution. Despite this slight increase in eddy KE, the KE of the mean flow is ~8% lower in the SOSE than in the first-guess solution. These changes are likely significant as the standard deviation of the KE over the 2-yr run is ~3%. That the mean flow KE decreased while the eddy KE increased is consistent with the theories (e.g., Marshall and Radko 2003), suggesting that eddies are responsible for slumping Southern Ocean isopycnals and decelerating the mean flow of the ACC system.

The mean SOSE atmospheric temperature is colder than the reanalysis fields equatorward of the ACC, yet warmer over most of the polar gyres (Fig. 2c). There are exceptions to this pattern, however: for example, the mean atmospheric surface temperature over the northwestern Ross Sea was significantly reduced. Atmospheric surface temperature perturbations are highly variable in time (i.e., the standard deviation is of comparable magnitude to the mean, Figs. 2c,h). Changes to the shortwave radiation (not shown) reflect this same pattern of cooling and heating, and of increased variance near the pole.

Optimization generally increases rainfall in the subtropical and polar gyres and decreases it over the ACC

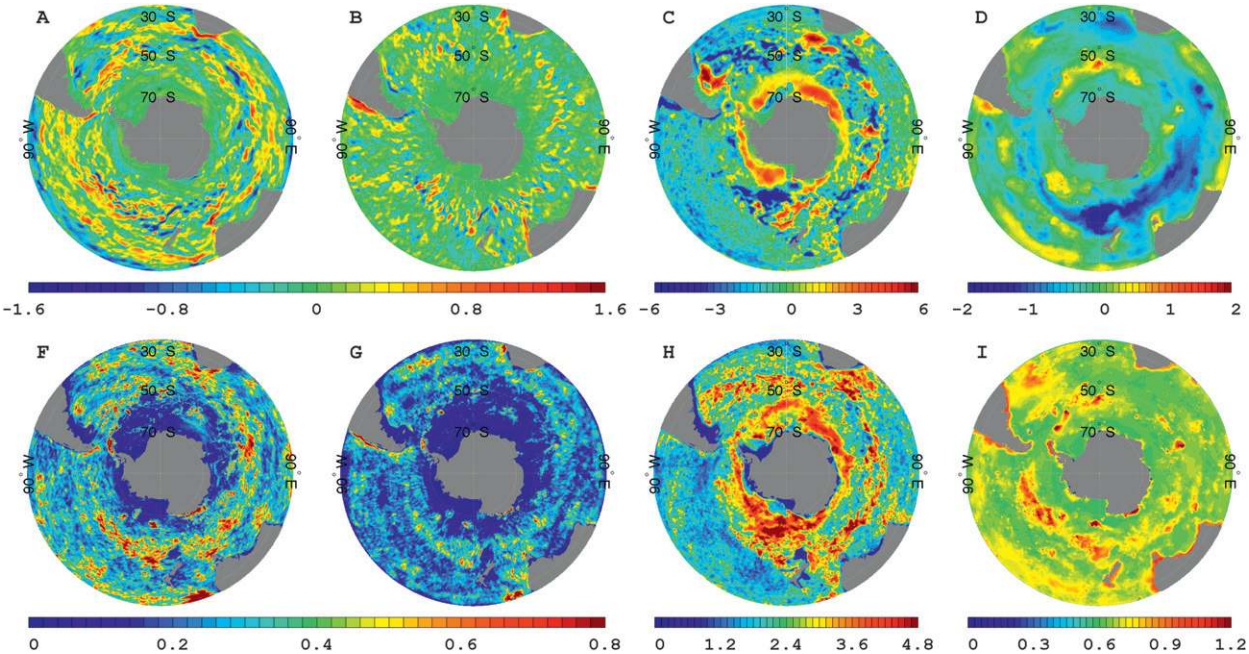

FIG. 2. The SOSE-determined atmospheric state fields minus the NCEP–NCAR fields: zonal wind speed (m s^{-1}) (a) time-mean difference and (f) standard deviation; meridional wind speed (m s^{-1}) (b) mean and (g) standard deviation; atmospheric temperature (°C) (c) mean and (h) standard deviation; and precipitation (mm day^{-1}) (d) mean and (i) standard deviation. Differences with respect to the shortwave radiative flux and the specific humidity are not shown. The optimized model inputs (i.e., the controls) are responsible for making the SOSE consistent with the observed ocean.

region (Fig. 2d). Temporal variations of atmospheric precipitation (Fig. 2i) and humidity (not shown) are greater in the SOSE than in the NCEP–NCAR reanalysis fields, with the greatest spectral energy increase in the hydrological cycle. Evaporation minus precipitation in the SOSE is larger than the NCEP–NCAR reanalysis in austral summer and smaller in austral winter. Furthermore, this hydrological cycle intensification in the SOSE is nearly uniform in space.

The SOSE atmospheric state is consistent with the NCEP–NCAR atmospheric state in that differences between the two are within the estimated NCEP–NCAR uncertainty. For comparison with the fields shown in Fig. 2, the average estimated uncertainty for the wind speed is ~4 m s^{-1}, for the atmospheric surface temperature ~12°C, and for the precipitation uncertainty ~5 mm day^{-1}. The deviations are, on average, less than 6% of the estimated uncertainties. That these differences are so small is surprising, and they suggest that modest deviations in the atmospheric state can greatly effect the solution and its consistency with observational constraints. The differences might, however, have proven more significant if error covariance information, and thus atmospheric state correlation information, were provided to the optimization system. Future work will use the method of Weaver and Courtier (2001) to provide these correlation scales.

4. Model–observation differences

A Southern Ocean general circulation model has been configured. State estimation machinery developed by the ECCO consortium enabled solving for initial conditions and an atmospheric state that, when prescribed to this ocean model, gives a solution consistent with the majority of 2005–06 observations. In this section, the consistency of the model solution, the state estimate, with the observations is assessed.

The magnitude of the misfit to both SST (here representing 5-m temperatures) infrared and microwave radiometer products is quite small, with 60% of the area having a mean misfit of less than 0.3°C (Figs. 3a,b). The expected uncertainty averages 0.4°C (the range is from 0.17° to 0.75°C with a spatial standard deviation over the domain of 0.14°C); thus the state estimate is largely within the expected uncertainty. There are, however, some notable biases. The estimate is too warm in the subtropics (despite the colder atmospheric temperature in this region in the SOSE compared to NCEP–NCAR). In ACC latitudes there are small-scale misfits owing to discrepancies in the frontal locations. There are two striking regions in the polar gyres where the estimate is O(1°C) warmer than the infrared observational product. Wintertime polynyas are generated in these regions by the SOSE but were not observed in either 2005 or 2006.

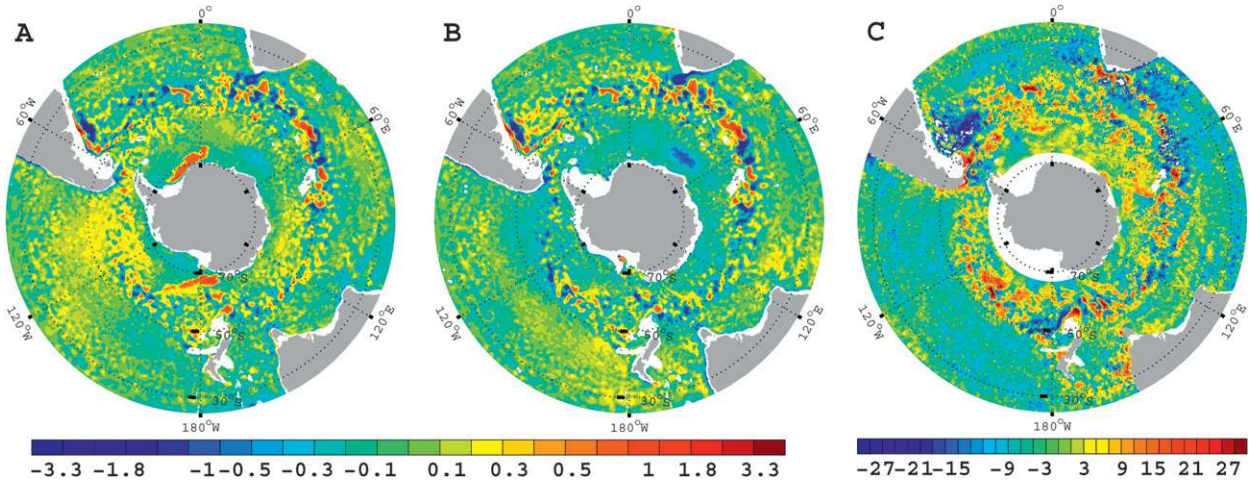

FIG. 3. Time-mean misfit: state estimate SST minus observed SST from (a) infrared and (b) microwave radiometer data. For infrared (microwave), 95% (94%) of the area has a misfit of less than 1°C and 61% (60%) is less than 0.3°C. The color axis is nonlinear. (c) The time average of the daily mean SSH from the state estimate differenced from the combined Gravity Recovery and Climate Experiment (GRACE) project dynamic ocean topography (Reigber et al. 2005) and T/P and *Jason-1* altimeter SSH anomaly observations. The units are centimeters and the color axis is linear.

Although these local deficiencies exist, the seasonal cycle of sea ice growth and retreat is captured and the integrated sea ice area tracks well with the observed value (Fig. 4). The first two months have the largest discrepancies because of the sea ice initial conditions. Neglecting these months, the average difference between the observed and estimated integrated sea ice area is 11%. In austral winter, the SOSE has slightly greater sea ice concentration than observed in the Ross Sea and slightly less than observed in the Weddell Sea.

The combined model–data uncertainty assigned to the TOPEX/Poseidon and *Jason-1* altimetric sea surface height (SSH) anomaly [sea level anomaly (SLA)] observations is spatially varying but on average is approximately 10 cm and dominated by eddy noise (i.e., representation error, Ponte et al. 2007). No fit to individual eddies was attempted, meaning relatively large small-scale misfits were allowed. Representation error is largest in the Antarctic Circumpolar Current region, which is characterized by especially high levels of eddy activity and large meandering fronts. The local time-mean misfits in this ACC region reach values of ~30 cm (Fig. 3c). Outside of the ACC region, the time-average misfit is, for the most part, much less than 10 cm and

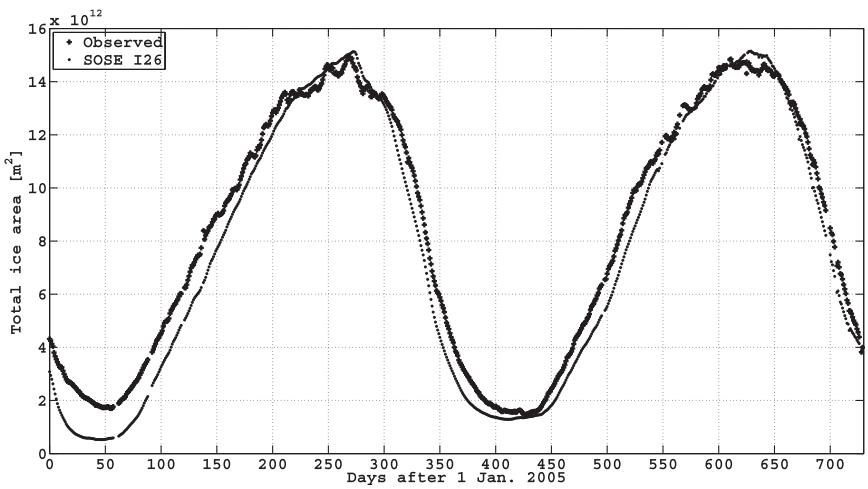

FIG. 4. Total sea ice area in the Southern Ocean: observed from NSIDC (pluses) and estimated (points). Regions where there are no observations are masked out in the integration. The seasonal change is slightly stronger and more rapid in the estimate than in the observations. Neglecting the first two months, the average difference in the two curves is approximately 11%.

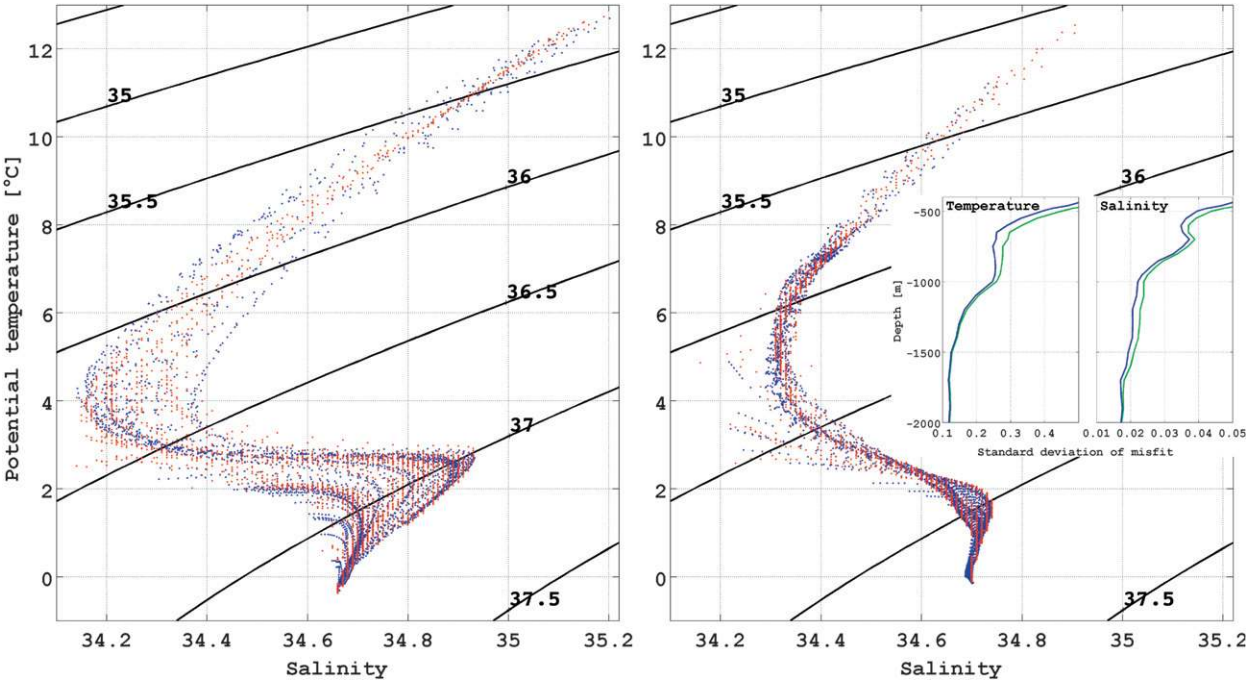

FIG. 5. Temperature and salinity (*T*–*S*) space plot for CTD synoptic sections taken in January and February 2005 (a) from 60° to 25°S at 30°W in the South Atlantic Ocean and (b) from 71° to 25.5°S at 150°W in the South Pacific Ocean. The top 400 m have been omitted for ease of water mass visualization. Potential density contours (referenced to 2000 dB) are plotted. The SOSE values are plotted in blue, and the observations are plotted in red. The state estimate water masses are slightly more spread in *T*–*S* space, suggesting an overly diffusive solution. The inset shows the standard deviations of the (left) temperature (°C) and (right) salinity misfits as a function of depth (between 500 and 2000 m) for the unoptimized run (green) and the SOSE (blue). The cost (i.e., weighted misfit squared) with respect to these sections was reduced 33% for temperature and 62% for salinity.

deemed acceptable. The same conclusion can be drawn for the European Remote Sensing Satellite (ERS) and *Geosat Follow-On* (*GFO*) altimetric observations (not shown, see Mazloff 2008).

Observed (CTD) synoptic sections are slightly tighter in *T*–*S* space than the state estimate (Fig. 5), suggesting that the estimate may be overemphasizing the degree of mixing. No large discrepancies are found, and the state estimate has no missing water masses in these meridional sections. Furthermore, there are no large clusters of points in the SOSE that are not in the observations, meaning no water masses have been added.

The cost (weighted misfit squared) of the SOSE to in situ observations is compared with that calculated from the *World Ocean Atlas 2001* (*WOA01*) climatological product (Stephens et al. 2001) and the 1° resolution state estimate of Forget (2010; Fig. 6). A cost much greater than one implies the model state is outside the uncertainty bounds prescribed. We have avoided discussing the prescribed uncertainty, as this is a complicated subject involving consideration of intrinsic model errors, observational measurement errors, and errors associated with the models representation of the ocean state (Forget and Wunsch 2007; Wunsch and Heimbach 2007). One can, however, gain an idea of the adequacy of the SOSE regardless of weighting by evaluating the relative costs. For each observational dataset shown, at almost all latitudes both state estimates are more consistent with the available observations for that year, particularly Argo, than the climatology. Much of what is known about the ocean comes from studies employing climatological products such as the *WOA01*. The Southern Ocean state estimate is, however, a better representation of the modern ocean than the *WOA01*, supporting its usefulness for analysis.

The SOSE is not completely consistent with the observed ocean; however, like all the ECCO state estimates, it is dynamically self consistent. No unphysical nudging terms are used. Furthermore, compared to essentially all other published eddy-permitting Southern Ocean simulations, only the SOSE has quantified misfits to most of the available satellite and in situ observations for this period. The conclusion drawn is that this eddy-permitting model solution is a reasonable estimate of the 2005–06 Southern Ocean state and can be used for understanding the regional circulation. Many of the remaining discrepancies noted will be removed through continued iteration. Other improvements can be made

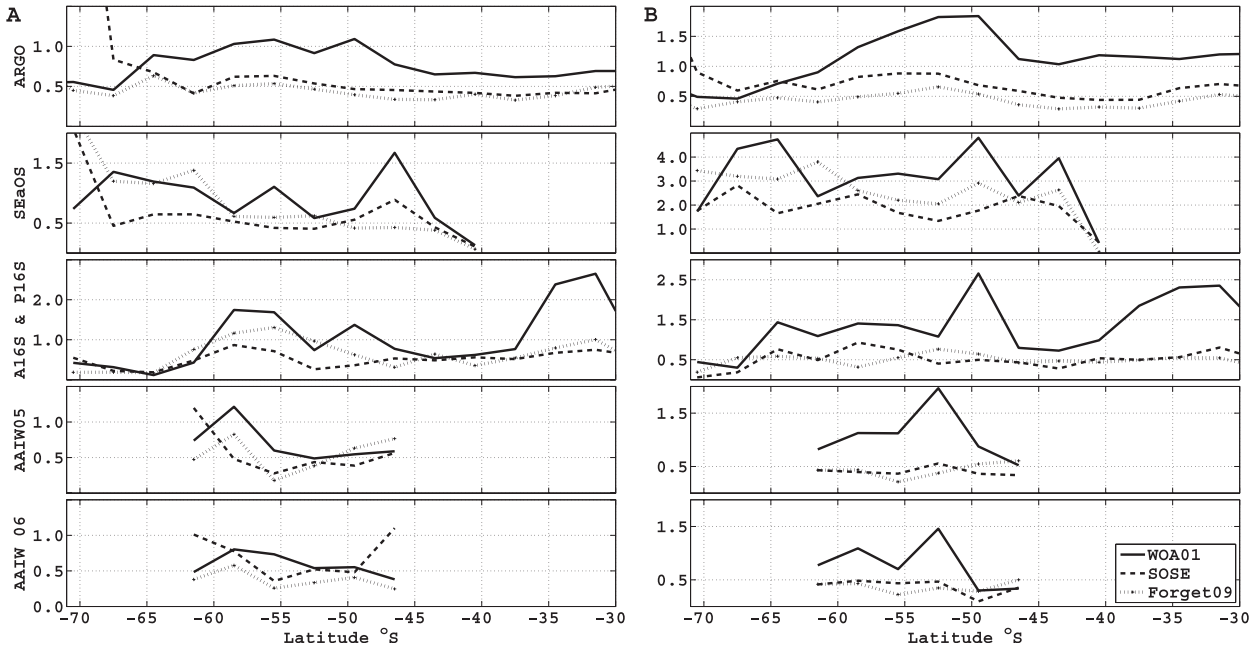

FIG. 6. The median cost value (weighted misfit squared) for the *WOA01* (solid line), a coarse-resolution state estimate (dotted line, Forget 2010), and the SOSE (dashed line) with respect to latitudinal bins of various in situ (a) temperature and (b) salinity observations: the in situ observational datasets are, from (top) to (bottom), the Argo project, the SEaOS project, combined A16 and P16 hydrographic sections, and two hydrographic sections from the Antarctic Intermediate Water Formation in the Southeast Pacific project (AAIW 2005 and 2006; for more information, see online at http://tryfan.ucsd.edu/aaiw/aaiw.htm). For the most part, the SOSE exhibits lower cost than the *WOA01*, implying that the state estimate is more consistent with this large influx of modern data.

by improving model physics, attaining more observations, and determining better estimates of the weights in what is evidently an asymptotic process.

5. The Southern Ocean circulation

Here we use the best available estimate to quantify the circulation and its corresponding property transports, leaving other analyses, for example, of water mass formation and evolution, for future work. In particular, the dynamics governing the meridional overturning circulation (MOC) are the subject of a companion paper by M. R. Mazloff and R. Ferrari (2010, unpublished manuscript) that relies on this estimate. Determining formal uncertainty estimates for the SOSE circulation analysis is also left for future work. A measure of uncertainty is provided, nevertheless, through the temporal standard deviations for calculated transports. In a Gaussian field, one standard deviation corresponds to about a 67% confidence interval; thus, in comparing values, the high probability of a true value outside the standard error must be kept in mind.

a. Horizontal volume transport

The time-mean Southern Ocean volume transport, as diagnosed from the state estimate, is shown in terms of a vertically integrated streamfunction ψ (Fig. 7) calculated by taking the vertical integral of the temporal mean zonal velocity and then integrating meridionally from the pole to the latitude plotted. From continuity, $U = -\psi_y$ and $V = \psi_x$, where U and V are the vertically integrated zonal and meridional velocities, and the horizontal transport is found by taking the difference between two streamlines.

1) STRUCTURE AND MAGNITUDE

The cyclonic Ross and Weddell polar gyres are found poleward of approximately 55°S (Fig. 7). Both gyres exhibit recirculations: see the double-peak feature in the time-mean transports (Fig. 8). The westward continental boundary current, the so-called Antarctic Polar Slope Current, which flanks much of the Antarctic continent (Orsi et al. 1995), is not apparent in Fig. 7; the transport associated with it in the SOSE is rather small, <10 Sv (Sv $\equiv 10^6$ m^3 s^{-1}). This along-continent westward current is apparent, however, as part of the polar gyres.

Transports associated with the anticyclonic subtropical gyres can be seen in the northern part of the domain of Fig. 7. The subtropical gyres transport approximately 30 Sv in the Atlantic and Pacific Oceans and approximately 60 Sv in the Indian Ocean. These transport volumes given are very rough estimates: the western boundary

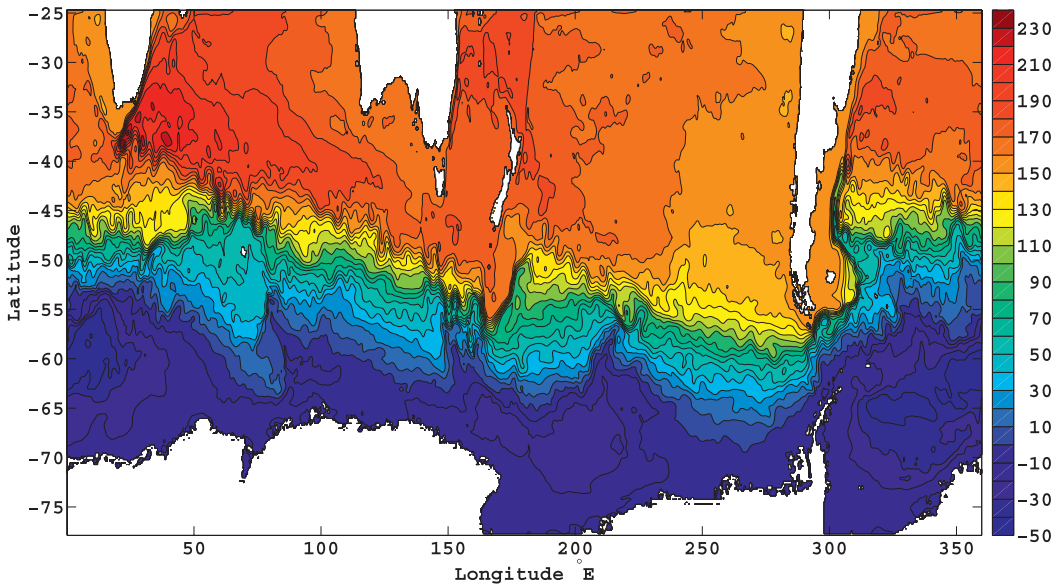

FIG. 7. Mean vertically integrated transport streamfunction (Sv) from the SOSE. The zero contour is the Antarctic coast, and the contour interval is 10 Sv. At the top of the plot, in red–orange, are the anticyclonic subtropical gyres. The Indian subtropical gyre transport is greater than the gyre transports of the Atlantic and Pacific subtropical gyres. At the bottom of the plot, in dark blue, are the cyclonic polar gyres. The Weddell gyre (~295° to ~50°E) transport (40 ± 8 Sv) is double the Ross gyre (~150° to ~240°E) transport (20 ± 5 Sv). Between the polar and subtropical gyres is the strong eastward transport of the ACC system (in blue–orange, see Fig. 9a for transport values). This current tracks poleward over the south Indian and South Pacific Oceans. Its equatorward excursions are abrupt, with the Falkland (or Malvinas) Current (~310°E) being the most significant meridional shift.

current of these gyres exhibit significant recirculations, and it is difficult to discern where the recirculations end and the gyres begin. The time-average transport of the Agulhas Current reaches 86 ± 64 Sv near its southern terminus (about 38°S, 22°E). The East Australian Current time-averaged transport reaches 31 ± 25 Sv at about 33°S, 154°E, and the time-averaged transport of the Brazil Current reaches 42 ± 29 Sv at about 40°S, 307°E.

Between the anticyclonic subtropical gyres and the cyclonic polar gyres is the massive mean eastward transport of the Antarctic Circumpolar Current. The ACC transport is best observed at its three most constricted meridional sections: below Africa [the World Ocean Circulation Experiment (WOCE) southern repeat section 2 (SR2)], below Tasmania (SR3), and below South America (SR1). The transport through these sections as a function of time (Fig. 9a) shows a significant seasonal cycle and a slightly larger mean transport in 2006. The transport is larger through SR3 owing to the Indonesian Throughflow (ITF) transport of 11 ± 1 Sv. Apart from this offset, the time series track closely, with each longitudinal section largely reflecting variations at all others.

2) COMPARISON WITH PREVIOUS ESTIMATES

Early estimates of the Weddell gyre transport suggested that it was greater than 20 Sv (Reid 1994), likely 30–50 Sv (Schröder and Fahrbach 1999). A recent static inverse model found a Weddell gyre transport of 45 Sv, Sultan et al. (2007), but without an error estimate. The 40 ± 8 Sv time-average Weddell gyre transport across 9°E found in the SOSE is consistent with these previous results. Reid (1997) estimated the Ross gyre transport to be 20 Sv (no error estimate given), consistent with the 20 ± 5 Sv average transport across 173°E found in the SOSE.

The first modern estimate of the ACC transport came from the International Southern Ocean Study (ISOS), 1974–81. Data in Drake Passage led to large inferred ranges of possible ACC transports. A reanalysis of the ISOS data was carried out by Cunningham et al. (2003), who found that a value of 134 ± 11 Sv was reasonable but error bounds for the estimate may be as large as ±27 Sv.

Static inverse models are consistent with the ISOS estimate, although they do tend to produce slightly larger mean ACC transport. For example, MacDonald and Wunsch (1996) obtained 142 ± 5 Sv, Ganachaud

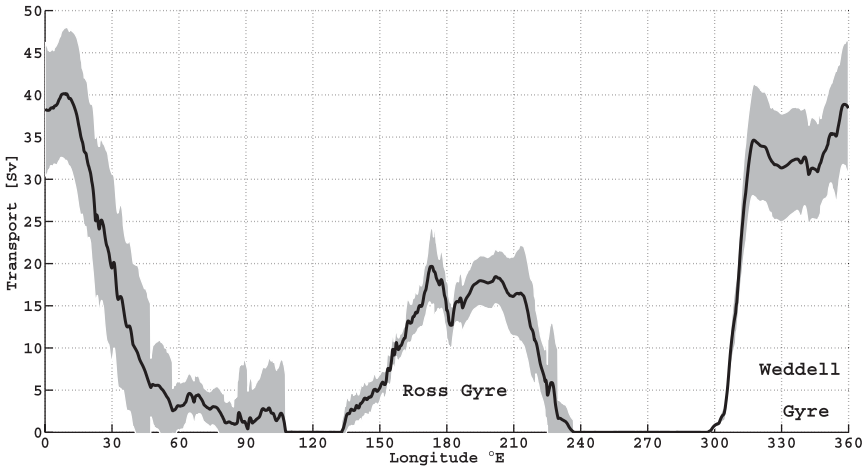

FIG. 8. The time-mean transport (Sv) of the polar gyres in the state estimate (thick line). Values within one standard deviation of this mean are shaded. The maximum Weddell gyre time-mean transport is 40 ± 8 Sv, while the maximum Ross gyre time-mean transport is about half that at 20 ± 5 Sv. The structure of both gyres can be seen in Fig. 7.

and Wunsch (2000) obtained 140 ± 6 Sv, and Sloyan and Rintoul (2001) calculate a transport of 135 ± 1 Sv. The state estimate produces a 2-yr mean ACC transport of 153 ± 5 Sv (Fig. 9a), which is on the high side of the ISOS estimate but within the error bounds estimated by Cunningham et al. (2003). Transport estimates south of Australia (SR3) are larger than in Drake Passage by 10–20 Sv owing to the ITF [e.g., Ganachaud and Wunsch (2000) find 157 ± 10 Sv and Rintoul and Sokolov (2001) find approximately 147 ± 10 Sv relative to the ocean bottom], which is consistent with the SOSE value of 164 ± 6 Sv. Possible reasons why the values inferred from the ISOS observations are lower than the SOSE value include the underestimation in the ISOS calculation of the abyssal flows (i.e., the reference level velocity may have been underestimated). Recent observations of abyssal currents in Drake Passage suggest that these flows may be stronger than previously thought, with near-bottom

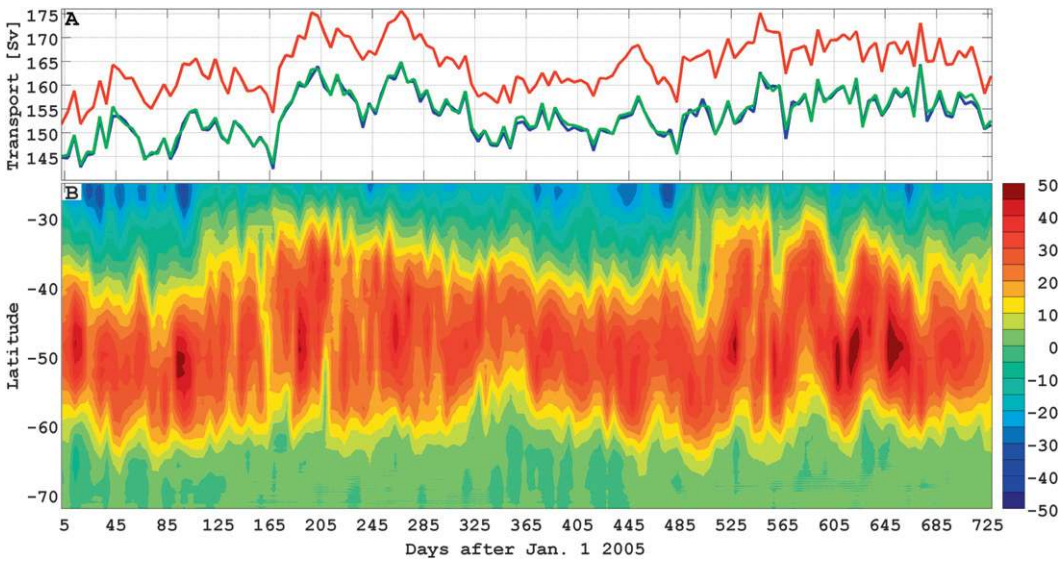

FIG. 9. (a) Time series of zonal transport (Sv) through the WOCE Southern Ocean repeat sections: Drake Passage (SR1, in blue), Africa to Antarctica (SR2, in green), and Australia to Antarctica (SR3, in red). The mean transports through the SR1, SR2, and SR3 lines are 153 ± 5 Sv, 154 ± 5 Sv, 164 ± 6 Sv (here, ± denotes temporal standard deviations). (b) Time series of ageostrophic transport (Sv) integrated zonally and vertically over the top 100 m. This transport, which peaks at 52 Sv, is driven by wind forced Ekman dynamics.

velocities averaging over 10 cm s^{-1} and high-speed events exceeding 60 cm s^{-1} (Chereskin et al. 2009).

The time period of the SOSE is one of positive southern annular mode (SAM) index (Nan and Li 2003). A positive SAM index, defined as the difference in the normalized monthly zonal-mean sea level pressure between 40° and 70°S (Gong and Wang 1999), is associated with stronger than average meridional SST gradients and westerly winds. The NCEP–NCAR reanalysis implies that the mean SAM index was 0.4 in 2005 and 1.1 in 2006. Annual-mean ACC transport in the SOSE is greater in 2006 than in 2005, consistent with this SAM index shift. ISOS took place during years marked by large SAM index shifts but was, on average, a time of negative SAM index. Shifts in the SAM index, and thus the ACC circulation, may be another reason why the SOSE transport estimate is on the high side of previous inferences. The time required to determine a truly stable mean value is unknown and could be very long.

b. *Meridional and vertical volume transport*

1) STRUCTURE AND MAGNITUDE

The meridional overturning circulation Eulerian streamfunction Ψ, $(\Psi_z, -\Psi_y) = (\oint v\,dx, \oint w\,dx)$, when displayed in depth space, shows the dominance of the strong Southern Ocean Ekman transport (Fig. 10a). Integrating the time-averaged SOSE ageostrophic meridional velocity in longitude and over the top 100 m shows it to peak at ~49°S with a value of 31 ± 8 Sv. This transport is primarily a wind-driven Ekman transport as near-surface ageostrophic flows arising from mechanisms besides wind stress account for only about 1 Sv of northward flow (and occur primarily just east of South America). Thus, the maximum time-mean wind-driven Ekman transport is estimated to be about 30 ± 9 Sv. Evaluation of the ageostrophic meridional transport in SOSE suggests that, while the temporally averaged and zonally integrated Ekman transport reaches depths of 80 m, ~50% of the transport occurs in the top 30 m.

Divergence of the significant Ekman transport appears to be supplied from depths reaching greater than 3000 m (Fig. 10a), composing the so-called Deacon cell (Döös and Webb 1994). The Ekman divergence is largely compensated adiabatically, however, by other forcing mechanisms (Speer et al. 2000). Taking the path of zonal integration along isopycnals (Fig. 10b) gives a better approximation of the true Lagrangian circulation and helps to demonstrate the adiabatic nature of the flow. Note, however, that no zonally integrated flow should be interpreted as depicting Lagrangian pathways: too much zonal structure exists (Nycander et al. 2002). Vertical motions in the volume-weighted isopycnal space overturning streamfunction are associated with either diabatic flows or changes in the stratification, that is, drift (see discussion at the end of this subsection). Neutral density γ is used in this work to limit compressibility effects in the isopycnal coordinate (McIntosh and McDougall 1996; Jackett and McDougall 1997).

The time-mean Southern Ocean Eulerian MOC comprises two cells (Figs. 10a and 10b). The bottom limb of the upper cell consists of an inflow of Upper Circumpolar Deep Water (UCDW, roughly $28.0 < \gamma < 28.1$), which enters the Southern Ocean between approximately 1000 and 2500 m. This UCDW upwells between 30°S and Drake Passage, mixing with newly formed Subantarctic Intermediate Mode Water (SAMW, roughly $26.6 < \gamma < 27.0$) to become Antarctic Intermediate Water (AAIW, roughly $27.0 < \gamma < 27.5$). AAIW flows equatorward near the surface forming the top limb of the upper cell. At the Subtropical Front (~37°S) this upper cell, and the AAIW, subduct beneath the surface overturning cell of the subtropical gyre.

The upper limb of the lower (abyssal) MOC cell is made up of a southward flow of Lower Circumpolar Deep Water (LCDW, roughly $28.1 < \gamma < 28.2$). LCDW flows into the polar gyres, mixes with cold shelf and surface waters, and forms Antarctic Bottom Water (AABW, roughly $28.2 < \gamma$). An equatorward flow of AABW makes up the bottom limb of the lower cell, which appears to be broken between 52° and 58°S in Fig. 10b. As stated above, vertical deviations in streamlines are associated with either diabatic flows or temporal changes in the stratification. An analysis of the continuity equation showed that this apparent break in the SOSE overturning is due to the latter: stratification of the solution is changing in time, which results in the projection of the flow in γ space to change. In essence, the change in stratification moves the coordinate system, or the "window," in time through which we are diagnosing the flow. As the flow is strongly sheared, moving the viewing window causes the apparent break in the lower cell. The cause of the stratification change in this abyssal location is uncertain, though a possible candidate is an inconsistency between the atmospheric forcing and the prescribed open northern boundary condition. If this is the case, making the northern boundary condition a control parameter, as is planned for future work, may remedy the situation. A lack of abyssal constraints, with only CTD observations going below 2000 m, is also a great hindrance to progress.

2) COMPARISON WITH PREVIOUS ESTIMATES

The deep overturning across 32°S in the state estimate of 13 ± 6 Sv is consistent with previous inverse calculations of 22 ± 5 (Talley et al. 2003) and 13 ± 4 Sv (Lumpkin and Speer 2007). The intermediate overturning

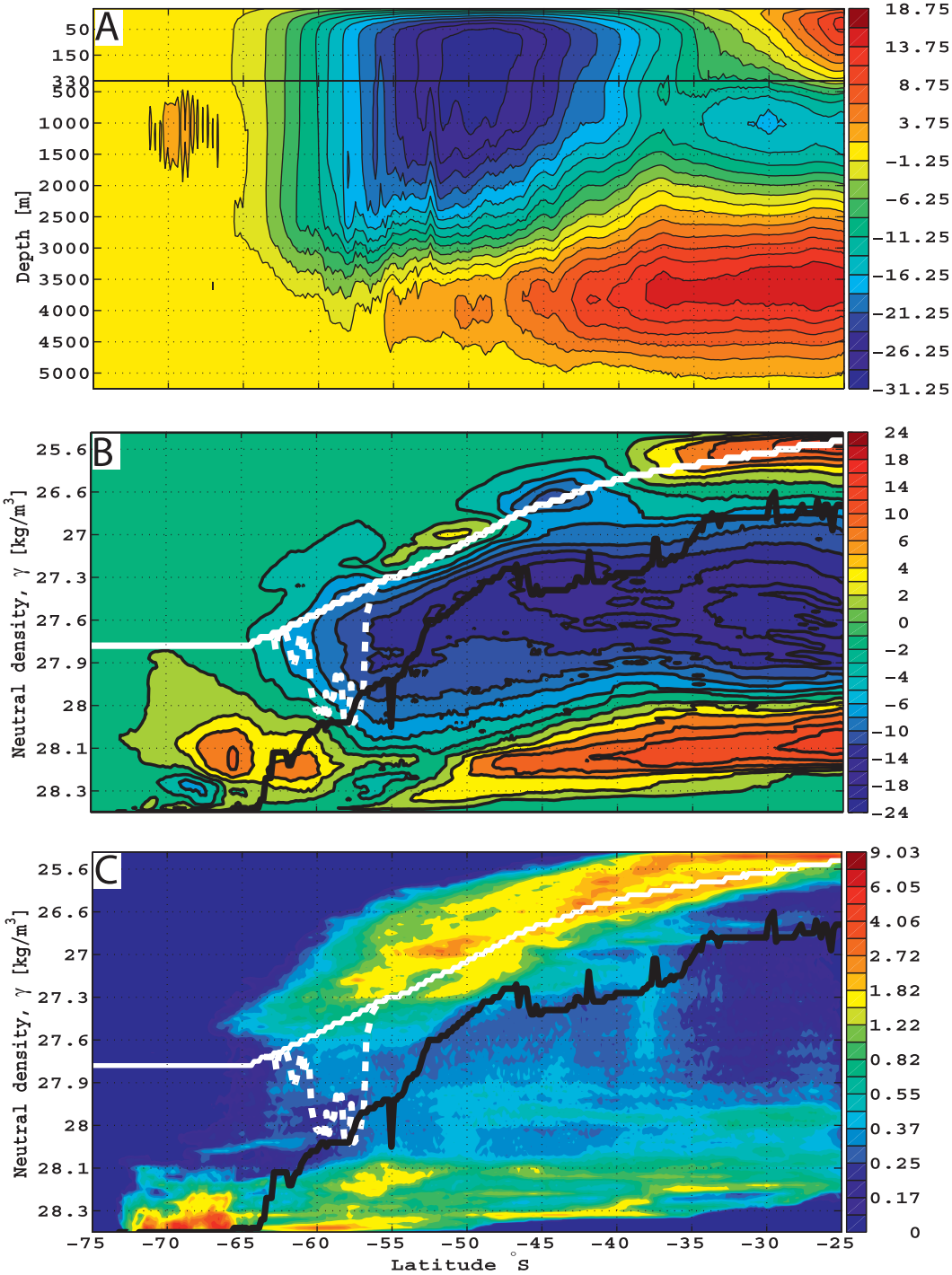

FIG. 10. Southern Ocean overturning streamfunction (Sv). (a) Latitude vs depth with a 2.5-Sv contour interval starting at ±1.25: The vertical axis is stretched for depths above 328 m. Positive (negative) values denote counterclockwise (clockwise) circulations. (b) Latitude vs neutral density: The contour intervals are stretched as shown in the color axis, and the vertical axis is stretched in γ space by a factor that reflects the volume of water at each density class (i.e., approximately the same value of water is found between each γ tick mark). The solid white line shows the approximate mean location of the surface. The solid black line shows the longitudinal and temporal maximum 5-day mean mixed layer γ at each latitude, revealing the significant extent of outcropping in the Southern Ocean. The dashed white line shows the approximate bounds of latitude circles that do not intersect bottom topography. Vertical deviations of streamlines are associated with either diabatic flows or changes in the stratification (see text). (c) The standard deviation of the zonally integrated volume-weighted meridional transport at each density class $\oint vh\,dx$ [i.e., the standard deviation of the γ derivative of (b)] in Sv: This is the variability of the transport in each density class. Determining the overall magnitude of transport variability is done by integrating over density ranges and reveals that the standard deviation of the overturning magnitude often exceeds 10 Sv.

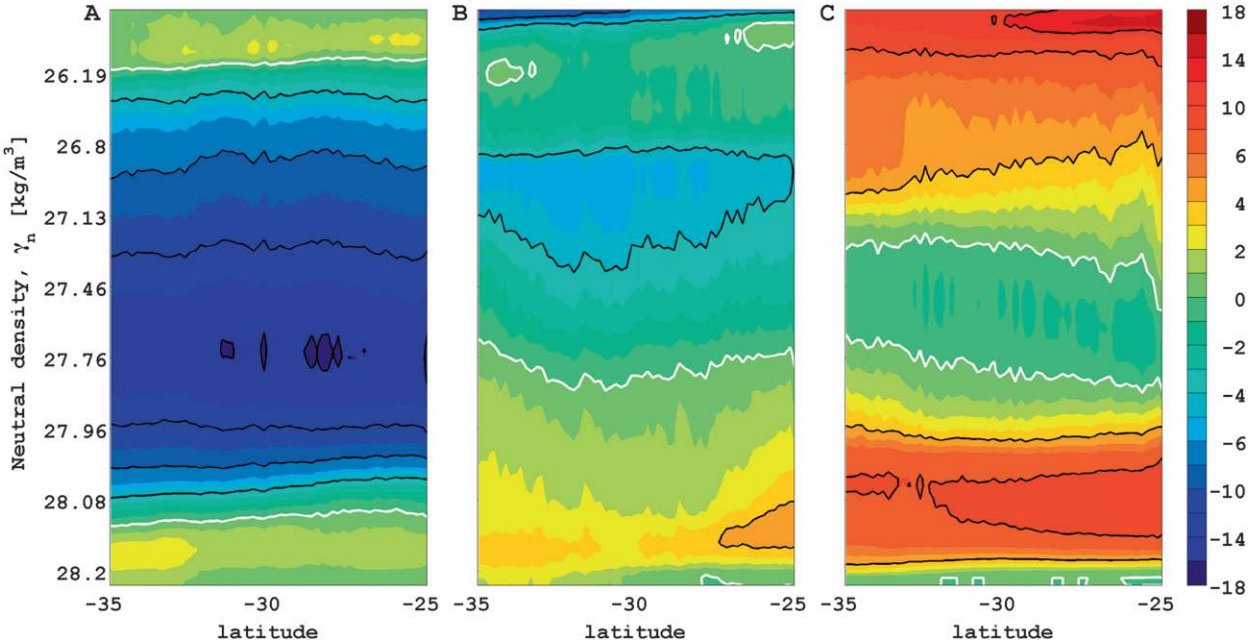

FIG. 11. Overturning streamfunction (Sv) for the (a) South Atlantic, (b) south Indian, and (c) South Pacific Oceans plotted in neutral density γ space. Positive (negative) values denote counterclockwise (clockwise) circulations. The contour interval is 4 Sv, and the zero contour is plotted in white. The vertical axis is stretched in γ space. The color axis is also stretched.

is 17 ± 12 Sv, and this value is also consistent, though slightly larger, than previous estimates [e.g., Talley (2003) finds an overturning of about 12 ± 5 Sv and Lumpkin and Speer (2007) find about 13 ± 7 Sv]. The upper overturning cell is approximately 12 ± 12 Sv across 32°, also consistent, though slightly larger, than previous static inverse model estimates [e.g., Lumpkin and Speer (2007) find an overturning of about 7 Sv; no error estimate was given]. The static inverse models are consistent with the state estimate to within its variability, which is all that should be expected—as the static inversions represent snapshots at best.

The overturning streamfunction found here is qualitatively like those found in FRAM (Döös and Webb 1994) and OCCAM (Lee and Coward 2003). One difference is that the SOSE produces a stronger overturning at depth than FRAM. Both FRAM and OCCAM produce a negligible overturning poleward of 65°S, whereas an overturning of 13 ± 4 Sv is shown here. This value is consistent with the magnitude of deep-water formation inferred from the static inverse models [13 ± 4 Sv in Lumpkin and Speer (2007) and 21 ± 6 Sv in Ganachaud and Wunsch (2000)]. It is possible that the lack of an abyssal cell in the unconstrained models is caused by poor representation of polar ocean processes and, thus, a failure to create AABW. As explained above, however, the negligible lower MOC cell in the high latitudes of these models may also be a symptom of the stratification changing in time. These issues, along with many other issues (e.g., regarding the level of interior mixing) highlight the need to constrain and test model representations of ocean states.

The meridional overturning streamfunctions for the southern regions of the Atlantic, Indian, and Pacific Oceans are considered to better estimate the transport of water masses flowing into and out of the Southern Ocean (Fig. 11). In the South Atlantic there is a 5 ± 2 Sv AABW abyssal outflow and a 20 ± 4 Sv deep-water inflow. These values, along with the upper-ocean estimated transports, are consistent with the static inverse model estimates of Ganachaud and Wunsch (2000) and Lumpkin and Speer (2007). The bottom-water exports to the Indian Ocean (6 ± 3 Sv) and the Pacific Ocean (10 ± 3 Sv) are also consistent with previous inferences (Ganachaud and Wunsch 2000). The deep-water imports to the Southern Ocean from the Indian Ocean (5 ± 5 Sv) and the Pacific Ocean (10 ± 7 Sv) are consistent with Ganachaud and Wunsch (2000), who find 11 ± 4 Sv and 7 ± 2 Sv, respectively. Though consistent, some of the largest discrepancies between this calculation and that of Ganachaud and Wunsch (2000) occur in the calculated volume exchanges of deep, intermediate, and surface water classes between the Southern Ocean and the Indian and Pacific Oceans, possibly attributable to a different Indonesian Throughflow estimate. The implicitly prescribed ITF transport used in SOSE is from

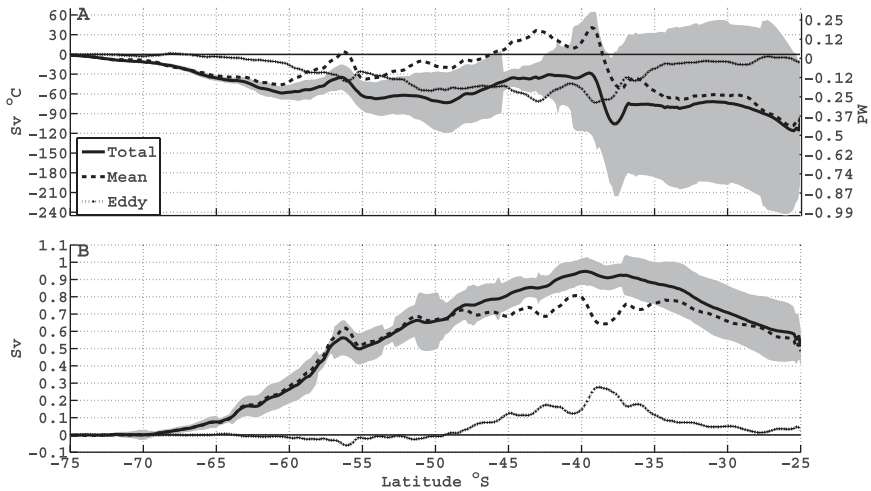

FIG. 12. (a) The northward (zonally integrated and time-mean) flux of heat (PW) and (b) the freshwater anomaly (relative to 35) (Sv) for the SOSE. The time-mean (dashed line), time-variable (dotted line), and total (solid line) fluxes are given. The shaded region indicates the 95% confidence interval for the total flux. The number of degrees of freedom in the record was determined from evaluation of the decorrelation time scale at each latitude.

Forget (2010) and is lower than the estimate of Ganachaud and Wunsch (2000): 11 ± 1 Sv as opposed to 15 ± 5 Sv [Wunsch (2010), from the 16-yr global ECCO-GODAE estimate, denoted v3.75, finds 11.5 ± 2.4 Sv but with extended periods of larger value]. It appears that this dynamically complicated region holds great importance with respect to the transport of most water classes between the Indian, Pacific, and Southern Oceans.

c. *Freshwater anomaly and temperature transport*

1) STRUCTURE AND MAGNITUDE

The meridional transports of freshwater anomaly and temperature are plotted as a function of latitude for global and regional zonal integrals (Figs. 12, 13). They have been decomposed into time-mean and transient components, $\overline{vT} = \overline{v}\,\overline{T} + \overline{v'T'}$ and $\overline{vF} = \overline{v}\,\overline{F} + \overline{v'F'}$, where an overbar represents the time mean and a prime the deviation from this mean; v is meridional velocity; T is temperature; and $F \equiv (35 - S)/35$ is the freshwater anomaly, where S is salinity. In the global integral, all latitudes show poleward heat and equatorward freshwater anomaly transports. Freshwater is carried primarily by the time-mean flow at all latitudes, whereas the heat transport is mainly carried by the time-mean flow only in the latitudes of the polar and subtropical gyres (i.e., poleward of ~60°S and equatorward of ~35°S). In the ACC latitudes, where the time-mean volume transport has a strong equatorward Ekman component, the transient dynamics are responsible for the net poleward heat transport. The regional plots (Fig. 13) are calculated in the subtropical gyres where the Ekman flow is poleward and the transient eddy transport component is insignificant. The diminishing freshwater transport in the Indian Ocean region (Fig. 13e) is indicative of significant evaporation in that region (Talley 2008).

The Southern Ocean has a strong seasonal cycle, making it difficult to determine accurate annual-mean freshwater anomaly and temperature transports over the short SOSE time interval. Standard deviations for many of the budget terms (sea ice growth, surface fluxes, and regional storage rates) are larger than the time-mean values, making these mean values statistically indistinguishable from zero. To gain a better idea of the uncertainty in the meridional transports in Figs. 12 and 13, the 95% confidence interval was calculated by assuming that, for each time series, the first zero crossing of the autocorrelation sequence was, arbitrarily, the decorrelation time scale. The number of degrees of freedom in the records is determined by dividing the length of the record (two years) by the decorrelation time. A 95% confidence interval is then determined using the standard deviation of the record, the estimated number of degrees of freedom, and by assuming that the fluctuations are normally distributed about the mean.

The maximum number of degrees of freedom in the advective heat transport record, which approaches 50, occurs in the ACC latitudes between about 45° and 38°S. This latitude band is where the mean enthalpy (heat) transport is equatorward, and the eddy heat transport is most important. In these latitudes the decorrelation time for the heat transport drops to ~15 days, in contrast to an average decorrelation time of 92 days elsewhere with a standard deviation of 40 days. The freshwater

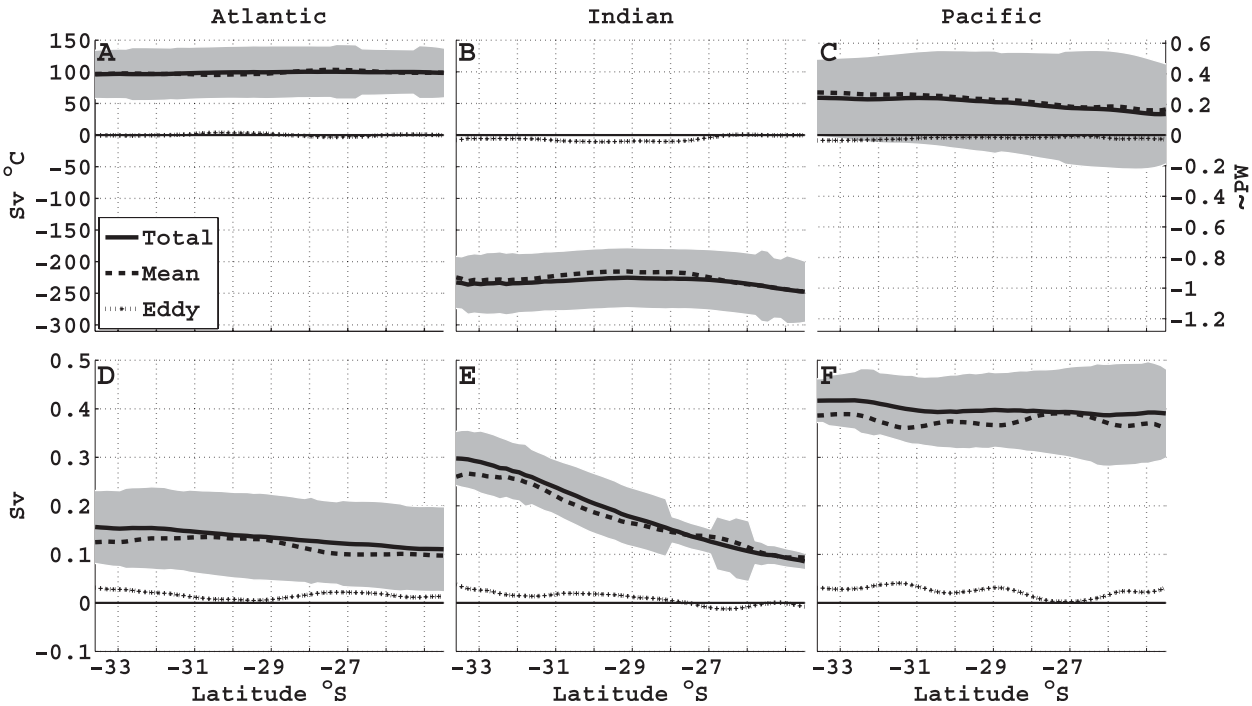

FIG. 13. (top) The northward (zonally integrated and time-mean) flux of temperature (Sv °C) and (bottom) the freshwater anomaly (relative to 35) (Sv) for the southern Atlantic, Indian, and Pacific Oceans. Except for the regional limits of the zonal integration, this figure is analogous to Fig. 12. The volume transport in these regional sections is nonzero; thus, the upper plots do not represent enthalpy (heat) transports.

anomaly transport decorrelation time is also highly variable, with an average of 86 days and a standard deviation of 41 days. Minima in the decorrelation times for the freshwater anomaly transports are, however, more evenly distributed spatially. The differences between mechanisms of heat and freshwater transport likely arise from the fact that heat transport is governed much more by near-surface dynamics.

The net meridional volume transport from the Southern Ocean to the tropics is negligible, though about 11 ± 1 Sv moves equatorward into the Pacific Ocean and returns from the Indian Ocean via the Indonesian Throughflow. This net poleward flow out of the Indian Ocean carries about 230 ± 80 Sv °C, making it the primary source of advective temperature anomaly transport into the Southern Ocean (here temperature anomaly transports are distinguished from enthalpy or heat transports because the net mass flux is nonzero). A compensating mean northward transport of approximately 100 ± 70 Sv °C into the Atlantic Ocean and 50 ± 130 Sv °C into the Pacific Ocean exists (Figs. 13a–c). The total temperature transport across 30°S is −73 Sv °C (∼−0.3 PW) with an estimated uncertainty of 126 Sv °C (∼0.5 PW, see Fig. 12a). Atmosphere–ocean temperature fluxes, occurring primarily in the South Pacific, account for approximately 30 Sv °C (∼0.1 PW), and the remaining temperature flux (approximately 40 Sv °C or ∼0.2 PW) becomes a (primarily south Indian Ocean) storage rate for the 2-yr estimate. Temporal standard deviations of both atmospheric fluxes and storage rates are an order of magnitude greater than the mean, making these inferred average values not significantly different from zero.

In contrast to the temperature fluxes, the freshwater anomaly budget exhibits smaller differences between basins. Freshwater input from the atmosphere occurs nearly uniformly across all regions and is balanced by an equatorward export. The time-mean freshwater anomaly transport across 30°S is 0.7 Sv with an estimated uncertainty of 0.2 Sv. This export to the tropics is most significant in the Pacific Ocean, likely due to the net volume flux out of this ocean along with its increased cross-sectional area (Figs. 13d–f). Time-mean zonal advective transports of freshwater anomaly are relatively steady at about 2.5 ± 0.1 Sv for all longitudes.

2) COMPARISON WITH PREVIOUS ESTIMATES

Previously estimated Southern Ocean heat loss rates to the atmosphere are larger than the ∼0.1 PW found here: 0.6 ± 0.3 PW (Ganachaud and Wunsch 2003), 0.46 ± 0.38 PW (Wijffels et al. 2001), and 0.8 ± 0.2 PW (Talley 2003). These previous estimates assumed a negligible ocean heat storage, however, whereas we find

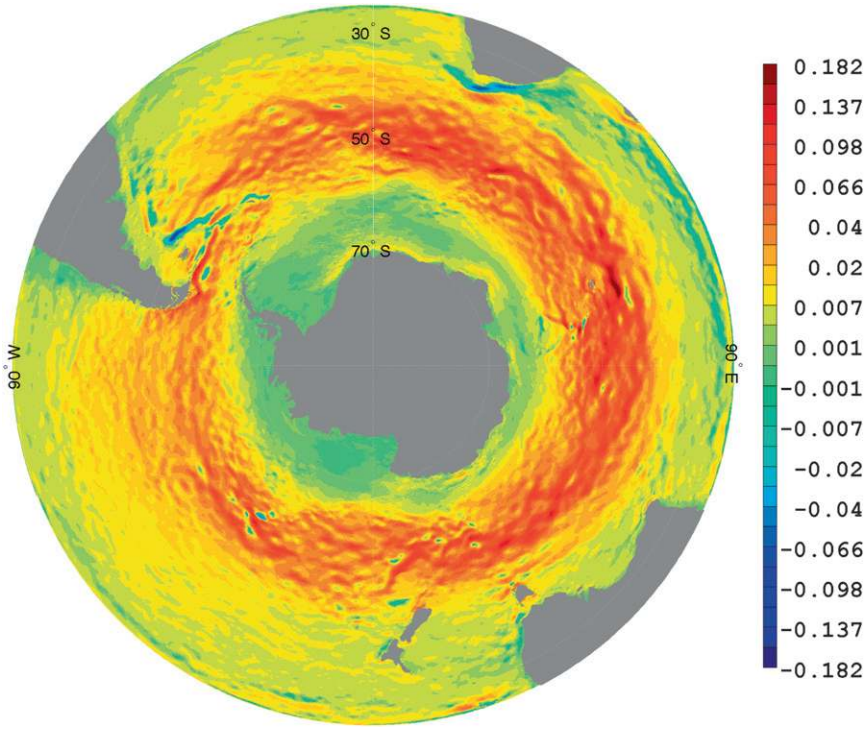

FIG. 14. Time-average rate of work (power) done by the wind on the Southern Ocean circulation, $\overline{\tau \cdot \mathbf{v}}$ (W m^{-2}). The integrated power input over the domain is 2.1 ± 1.1 TW. The color axis is nonlinear.

a ~0.2 PW storage rate. The divergence of the total heat transport shown in Fig. 12a may be used to infer the combined atmospheric flux and storage rate at each latitude.

Estimated regional temperature anomaly transports across ~30°S are consistent with previous static inverse model estimates. The state estimate finds 99 ± 66 Sv °C (or ~0.4 ± 0.3 PW) carried into the Atlantic Ocean, Ganachaud and Wunsch (2000) find a flux of about 0.3 ± 2 PW, Holfort and Siedler (2001) find 0.29 ± 0.24 PW, and Talley (2003) finds about 0.23 ± 0.05 PW. The combined temperature anomaly transport into the Indian and Pacific Oceans in the state estimate is 180 ± 210 Sv °C (~−0.8 ± 0.9 PW). For this region, Ganachaud and Wunsch (2000) and Wijffels et al. (2001) both find −0.9 PW (error bars not explicitly given) and Talley (2003) finds about −1.2 ± 0.2 PW.

The total freshwater transport out of the Southern Ocean is 0.7 ± 0.2 Sv in the SOSE. Freshwater anomaly storage is insignificant in the SOSE, so this transport rate is consistent with the net precipitation/runoff rate of 0.8 ± 0.9 Sv inferred by Ganachaud and Wunsch (2003). The equatorward export of freshwater across 32°S into the Atlantic and Indian Oceans is consistent with the findings of Talley (2008). This transport is 0.2 ± 0.1 Sv for both Atlantic and Indian Oceans in the SOSE, and Talley (2008) finds 0.215 ± 0.036 Sv and 0.257 ± 0.085 Sv for each respective region. The transport across 28°S into the Pacific Ocean, however, is inconsistent as the SOSE yields 0.4 ± 0.1 Sv and Talley (2008) inferred a transport of 0.136 ± 0.077 Sv. The discrepancy in the Pacific Ocean freshwater anomaly transport inferences suggests an underestimate of the uncertainty in either the current calculation, the Talley (2008) calculation based on shipboard data collected in June–July 1967, or both.

d. *Rate of wind work*

The ACC is largely aligned with the atmospheric winds, resulting in a large rate of work by the wind on the ocean (Wunsch 1998). Using the present estimate, the domain-integrated (over the area south of 25°S) rate of wind work done on the meridional and zonal velocities is 1.1 ± 0.9 and 1.1 ± 0.3 TW, respectively. The total integrated rate of wind work for the SOSE domain is 2.1 ± 1.1 TW (Fig. 14). Of this ~2 TW, only 0.5 ± 0.1 TW is absorbed by the (primarily zonal) geostrophic flow. The power transfer to the ageostrophic ocean circulation is approximately three times greater than that transferred to the geostrophic flow [Ferrari and Wunsch (2009, supplemental material) provide a wider context for these numbers].

The rate of wind work calculation is made using 6-hourly averaged fields. Smoothing the ocean velocity

fields by applying a 10-day running mean substantially reduces the power input by ~1.3 TW or ~62%. The rate of wind work remaining, which is done on the slowly varying ocean dynamics, is 0.8 ± 0.2 TW and is primarily input to the ACC zonal flow. In contrast, the power input removed by the temporal smoothing is significant everywhere the winds are strong. This mechanism of energy transfer, which is likely associated with inertial motions, does not rely on the presence of the ACC.

It has been proposed that a mechanism for dissipating eddy energy is through wind stress working against eddy surface flows (Zhai and Greatbatch 2007). When a large-scale wind field blows over an oceanic eddy, the stress acting in the direction of the oceanic flow is slightly, though systematically, reduced relative to that acting against the direction of the oceanic motion, thus resulting in an eddy spindown. Such effects can be a significant factor in the energy budget of mesoscale eddies (Zhai and Greatbatch 2007; Ferrari and Wunsch 2009). The meridional and zonal ocean speeds in the Southern Ocean are, on average, 5.1 ± 0.9% and 5.2 ± 0.9% of the magnitude of the wind velocities (this calculation was done by comparing ocean surface velocity magnitudes to atmospheric 10-m winds and then spatially and temporally averaging). Assuming a linear drag coefficient implies that ocean velocities could possibly reduce the rate of wind work budget over the SOSE domain by up to 12%.

6. Discussion

The adjoint methodology, as employed by the ECCO machinery, has been used here to estimate the Southern Ocean general circulation properties in the years 2005 and 2006. The resulting eddy-permitting state estimate is largely consistent with the observations, though improvements in the solution continue. Qualitative changes in the conclusions discussed here are not expected, although quantitative ones are. In general, the integrated freshwater, temperature, and volume transports in the state estimate are quantitatively consistent with previous inverse estimates; no gross inconsistencies exist. What has been accomplished is an improvement to the existing static inverse estimates through both increased resolution and the explicit accounting for the important time variability. Southern Ocean theories involving short temporal and spatial scale dynamics (e.g., involving decompositions into eddy-mean flow components) may now be tested with an eddy-permitting (dynamically and thermodynamically realistic) GCM solution that is known to be compatible with most the observational datasets available for this period.

The state estimate allows diagnosing the variability in the circulation. It is found, for example, that variability of the Ekman transport is significant in both space and time (Fig. 9b). The work of Rintoul and England (2002) suggests that these transport fluctuations will impact the formation rates and characteristics of water masses. Consistent with Wunsch and Heimbach (2009), it is found that strong temporal variability in the Southern Ocean is not limited to the near-surface flow. The standard deviation of the γ derivative of the γ-space MOC streamfunction (i.e., the zonally integrated volume-weighted meridional transport $\oint vh\,dx$) shows significant variability in both meridional overturning cells (Fig. 10c). These fluctuations account for temporal changes in the MOC O(10 Sv). The degree of outcropping occurring is substantial as well (Fig. 10b); surface densities on a latitude circle occasionally reach the UCDW density class and, thus, directly ventilate the lower branch of the upper MOC cell. It is often the case that the maximum surface density differences in time, or along latitude circles, is greater than the differences between the mixed layer and the ocean floor.

Resolving the variability of the Southern Ocean circulation now leaves one with the task of explaining it. Questions arise as to why recirculations appear to have a minimal impact on the integrated ACC transport, yet significantly affect the subtropical and polar gyre transports. The temporal standard deviation of the ACC transport is ~6 Sv, or 0.4% of the transport magnitude, whereas the standard deviations of the Ross and Weddell gyre transports are 8 Sv and 5 Sv (20% and 25% of the transport magnitudes), respectively. Similarly, the recirculations in the subtropical gyre western boundary currents result in the standard deviations of these transports being approximately 75% of the average magnitude. It is not clear why there is insignificant divergence and storage of ACC waters occurring in each of the major Southern Ocean basins.

Future efforts will focus on illuminating the dominant physical mechanisms at work in the estimate of the three-dimensional time-evolving flow presented here. Simultaneous efforts will focus on reducing the remaining inconsistencies of this general circulation model solution with the massive constraining dataset (e.g., through further iterations of the adjoint method). The 2-yr time interval of estimation is much too short to detect trends in the system, and another intended improvement to the SOSE is the extension of the temporal duration through 2009, thus encompassing the International Polar Year (IPY from March 2007 to March 2009). Additional in situ observational constraints are being acquired, and cost terms penalizing discrepancies between modeled and observed sea ice concentration are being added.

As in any least squares optimization, the solution is determined by the weighting. Calculating appropriate uncertainties (weights) for use in coarse-resolution (non-eddying) state estimation is a serious outstanding problem (Forget and Wunsch 2007). Calculating appropriate uncertainties for use in an eddy-permitting state estimate is even more challenging. Having eddy signals in both model and observations can increase the expected misfit. Future work must determine the best way to constrain eddy-resolving state estimates to observations. This effort includes determining the cost function structure. For example, is it desirable and feasible to reproduce the ocean eddy field, or is it wiser to reproduce only the eddy statistics (Köhl and Willebrand 2002; Lorenc and Payne 2007)?

The SOSE will benefit from the continually occurring improvements to the ECCO state estimation infrastructure. These improvements range from better forward model parameterizations to a better designed cost function. Yet another planned improvement for the SOSE will be the use of a smoothness operator to ensure a degree of correlation in the determined forcing fields and thus yield more realistic scales in the model inputs (Weaver and Courtier 2001). The implementation of northern boundary controls is also planned (Hoteit et al. 2005). It is the hope that a continued influx of Southern Hemisphere observations combined in this ever-improving model synthesis framework will lead to a greater understanding of this important part of the global ocean circulation and climate.

Acknowledgments. We are grateful to the very large group of oceanographers who collected and processed the observations used here, without whom none of this would be possible. The members of the ECCO-GODAE group at MIT and AER were essential to the carrying out of this work. Particular thanks are owed to Gael Forget and Charmaine King for help in carrying out the state estimate. The work was supported through NOPP with main funding from NASA and was made possible through significant computational resources provided by the National Science Foundation through TeraGrid resources provided by San Diego Supercomputer Center under Grant MCA06N007. NCAR computer resources were also helpful. Mazloff would like to thank Teresa Chereskin for postgraduate support under NSF Grant OCE 0327544.

REFERENCES

Boehme, L., M. P. Meredith, S. E. Thorpe, M. Biuw, and M. Fedak, 2008: Antarctic Circumpolar Current frontal system in the South Atlantic: Monitoring using merged Argo and animal-borne sensor data. *J. Geophys. Res.,* **113,** C09012, doi:10.1029/2007JC004647.

Chelton, D. B., R. A. deSzoeke, M. G. Schlax, K. El Naggar, and N. Siwertz, 1998: Geographical variability of the first baroclinic Rossby radius of deformation. *J. Phys. Oceanogr.,* **28,** 433–460.

Chereskin, T. K., K. A. Donohue, D. R. Watts, K. L. Tracey, Y. L. Firing, and A. L. Cutting, 2009: Strong bottom currents and cyclogenesis in Drake Passage. *Geophys. Res. Lett.,* **36,** L23602, doi:10.1029/2009GL040940.

Conkright, M. E., R. Locarnini, H. E. Garcia, T. O'Brien, T. Boyer, C. Stephens, and J. Antonov, 2002: *World Ocean Atlas 2001: Objective Analyses, Data Statistics, and Figures*. National Oceanographic Data Center, CD-ROM documentation, 17 pp.

Crease, J., 1964: The Antarctic Circumpolar Current and convergence. *Proc. Roy. Soc. London,* **281A,** 14–21.

Cunningham, S. A., S. G. Alderson, B. A. King, and M. A. Brandon, 2003: Transport and variability of the Antarctic Circumpolar Current in Drake Passage. *J. Geophys. Res.,* **108,** 8084, doi:10.1029/2001JC001147.

Döös, K., and D. J. Webb, 1994: The Deacon cell and the other meridional cells of the Southern Ocean. *J. Phys. Oceanogr.,* **24,** 429–442.

Ferrari, R., and C. Wunsch, 2009: Ocean circulation kinetic energy: Reservoirs, sources, and sinks. *Annu. Rev. Fluid Mech.,* **41,** 253–282.

Forget, G., 2010: Mapping ocean observations in a dynamical framework: A 2004–06 ocean atlas. *J. Phys. Oceanogr.,* in press.

——, and C. Wunsch, 2007: Estimated global hydrographic variability. *J. Phys. Oceanogr.,* **37,** 1997–2008.

Ganachaud, A., and C. Wunsch, 2000: Improved estimates of global ocean circulation, heat transport and mixing from hydrographic data. *Nature,* **408,** 453–457.

——, and ——, 2003: Large-scale ocean heat and freshwater transports during the World Ocean Circulation Experiment. *J. Climate,* **16,** 696–705.

Gebbie, G., P. Heimbach, and C. Wunsch, 2006: Strategies for nested and eddy-resolving state estimation. *J. Geophys. Res.,* **111,** C10073, doi:10.1029/2005JC003094.

Giering, R., and T. Kaminski, 1998: Recipes for adjoint code construction. *ACM Trans. Math. Software,* **24,** 437–474.

Gilbert, J. C., and C. Lemaréchal, 1989: Some numerical experiments with variable-storage quasi-Newton algorithms. *Math. Program.,* **45,** 407–435.

Gille, S. T., and K. A. Kelly, 1996: Scales of spatial and temporal variability in the Southern Ocean. *J. Geophys. Res.,* **101,** 8759–8774.

Gong, D., and S. Wang, 1999: Definition of Antarctic Oscillation index. *Geophys. Res. Lett.,* **26,** 459–462.

Gordon, A. L., and E. J. Molinelli, 1982: *Southern Ocean Atlas*. Columbia University Press, 291 pp.

Gould, J., and Coauthors, 2004: Argo profiling floats bring new era of in situ ocean observations. *Eos, Trans. Amer. Geophys. Union,* **85,** doi:10.1029/2004EO190002.

Gouretski, V. V., and K. P. Koltermann, 2004: WOCE global hydrographic climatology. Berichte des Bundesamtes für Seeschifffahrt und Hydrographie Tech. Rep. 35, 52 pp.

Hibler, W. D., III, 1980: Modeling a variable thickness sea ice cover. *Mon. Wea. Rev.,* **108,** 1943–1973.

Holfort, J., and G. Siedler, 2001: The meridional oceanic transports of heat and nutrients in the South Atlantic. *J. Phys. Oceanogr.,* **31,** 5–29.

Hoteit, I., B. Cornuelle, A. Kohl, and D. Stammer, 2005: Treating strong adjoint sensitivities in tropical eddy-permitting variational data assimilation. *Quart. J. Roy. Meteor. Soc.,* **131,** 3659–3682.

Hughes, C. W., 2005: Nonlinear vorticity balance of the Antarctic Circumpolar Current. *J. Geophys. Res.,* **110,** C11008, doi:10.1029/2004JC002753.

——, M. P. Meredith, and K. J. Heywood, 1999: Wind-driven transport fluctuations through Drake Passage: A southern mode. *J. Phys. Oceanogr.,* **29,** 1971–1992.

Jackett, D. R., and T. J. McDougall, 1997: A neutral density variable for the world's oceans. *J. Phys. Oceanogr.,* **27,** 237–263.

Kalnay, E., and Coauthors, 1996: The NCEP/NCAR 40-Year Reanalysis Project. *Bull. Amer. Meteor. Soc.,* **77,** 437–471.

Killworth, P. D., 1992: An equivalent-barotropic mode in the Fine Resolution Antarctic Model. *J. Phys. Oceanogr.,* **22,** 1379–1387.

——, and M. M. Nanneh, 1994: Isopycnal momentum budget of the Antarctic Circumpolar Current in the Fine Resolution Antarctic Model. *J. Phys. Oceanogr.,* **24,** 1201–1223.

——, D. A. Smeed, and A. J. G. Nurser, 2000: The effects on ocean models of relaxation toward observations at the surface. *J. Phys. Oceanogr.,* **30,** 160–174.

Köhl, A., and J. Willebrand, 2002: An adjoint method for the assimilation of statistical characteristics into eddy-resolving ocean models. *Tellus,* **54A,** 406–425, doi:10.1034/j.1600-0870.2002.01294.x.

Large, W. G., and S. G. Yeager, 2004: Diurnal to decadal global forcing for ocean and sea-ice models: The data sets and flux climatologies. NCAR Tech. Rep. TN-460+STR, 112 pp.

Le Dimet, F.-X., and O. Talagrand, 1986: Variational algorithms for analysis and assimilation of meteorological observations: Theoretical aspects. *Tellus,* **38A,** 97–110.

Lee, M.-M., and A. Coward, 2003: Eddy mass transport for the Southern Ocean in an eddy-permitting global ocean model. *Ocean Modell.,* **5,** 249–266.

Lorenc, A. C., and T. Payne, 2007: 4D-Var and the butterfly effect: Statistical four-dimensional data assimilation for a wide range of scales. *Quart. J. Roy. Meteor. Soc.,* **133,** 607–614, doi:10.1002/qj.36.

Losch, M., D. Menemenlis, J.-M. Campin, P. Heimbach, and C. Hill, 2010: On the formulation of sea-ice models. Part 1: Effects of different solver implementations and parameterizations. *Ocean Modell.,* **33,** 129–144.

Lumpkin, R., and K. Speer, 2007: Global ocean meridional overturning. *J. Phys. Oceanogr.,* **37,** 2550–2562.

MacDonald, A. M., and C. Wunsch, 1996: An estimate of global ocean circulation and heat fluxes. *Nature,* **382,** 436–439, doi:10.1038/382436a0.

Marshall, J., and T. Radko, 2003: Residual-mean solutions for the Antarctic Circumpolar Current and its associated overturning circulation. *J. Phys. Oceanogr.,* **33,** 2341–2354.

——, A. Adcroft, C. Hill, L. Perelman, and C. Heisey, 1997: A finite-volume, incompressible Navier-Stokes model for studies of the ocean on parallel computers. *J. Geophys. Res.,* **102** (C3), 5753–5766.

Mazloff, M. R., 2008: The dynamics of the Southern Ocean meridional overturning circulation as diagnosed from an eddy permitting state estimate. Ph.D. thesis, Massachusetts Institute of Technology and the Woods Hole Oceanographic Institution, 127 pp.

McIntosh, P. C., and T. J. McDougall, 1996: Isopycnal averaging and the residual mean circulation. *J. Phys. Oceanogr.,* **26,** 1655–1660.

Nan, S., and J. Li, 2003: The relationship between the summer precipitation in the Yangtze River valley and the boreal spring Southern Hemisphere annular mode. *Geophys. Res. Lett.,* **30,** 2266, doi:10.1029/2003GL018381.

Nycander, J., K. Döös, and A. C. Coward, 2002: Chaotic and regular trajectories in the Antarctic Circumpolar Current. *Tellus,* **54A,** 99–106.

Olbers, D., D. Borowski, C. Völker, and J.-O. Wölff, 2004: The dynamical balance, transport and circulation of the Antarctic Circumpolar Current. *Antarct. Sci.,* **16,** 439–470.

Orsi, A. H., T. Whitworth, and W. D. Nowlin, 1995: On the meridional extent and fronts of the Antarctic Circumpolar Current. *Deep-Sea Res.,* **42,** 641–673.

Ponte, R. M., C. Wunsch, and D. Stammer, 2007: Spatial mapping of time-variable errors in *Jason-1* and TOPEX/Poseidon sea surface height measurements. *J. Atmos. Oceanic Technol.,* **24,** 1078–1085.

Reid, J., 1994: On the total geostrophic circulation of the North Atlantic Ocean: Flow patterns, tracers and transports. *Prog. Oceanogr.,* **33,** 1–92.

——, 1997: On the total geostrophic circulation of the Pacific Ocean: Flow patterns, tracers, and transports. *Prog. Oceanogr.,* **39,** 263–352, doi:10.1016/S0079-6611(97)00012-8.

Reigber, C., R. Schmidt, F. Flechtner, R. König, U. Meyer, K.-H. Neumayer, P. Schwintzer, and S. Y. Zhu, 2005: An Earth gravity field model complete to degree and order 150 from GRACE: EIGEN-GRACE02S. *J. Geodyn.,* **39,** 1–10.

Reynolds, R. W., N. A. Rayner, T. M. Smith, D. C. Stokes, and W. Wang, 2002: An improved in situ and satellite SST analysis for climate. *J. Climate,* **15,** 1609–1625.

Rintoul, S. R., and S. Sokolov, 2001: Baroclinic transport variability of the Antarctic Circumpolar Current south of Australia (WOCE repeat section SR3). *J. Geophys. Res.,* **106,** 2795–2814.

——, and M. H. England, 2002: Ekman transport dominates local air–sea fluxes in driving variability of Subantarctic Mode Water. *J. Phys. Oceanogr.,* **32,** 1308–1321.

——, C. W. Hughes, and D. Olbers, 2001: The Antarctic Circumpolar Current system. *Ocean Circulation and Climate,* G. Siedler, J. Church, and J. Gould, Eds., Academic Press, 271–302.

Saunders, P., and S. Thompson, 1993: Transport, heat and freshwater fluxes within a diagnostic model (FRAM). *J. Phys. Oceanogr.,* **23,** 452–464.

Schröder, M., and E. Fahrbach, 1999: On the structure and the transport of the eastern Weddell gyre. *Deep-Sea Res. II,* **46,** 501–527, doi:10.1016/S0967-0645(98)00112-X.

Sloyan, B. M., and S. R. Rintoul, 2001: Circulation, renewal, and modification of Antarctic Mode and Intermediate Water. *J. Phys. Oceanogr.,* **31,** 1005–1030.

Speer, K., S. R. Rintoul, and B. Sloyan, 2000: The diabatic Deacon cell. *J. Phys. Oceanogr.,* **30,** 3212–3222.

Stammer, D., and Coauthors, 2002: Global ocean circulation during 1992–1997, estimated from ocean observations and a general circulation model. *J. Geophys. Res.,* **107,** 3118, doi:10.1029/2001JC000888.

Stephens, C., J. I. Antonov, T. P. Boyer, M. E. Conkright, R. A. Locarnini, T. D. O'Brien, and H. E. Garcia, 2001: *Temperature*. Vol. 1, *World Ocean Atlas 2001,* NOAA Atlas NESDIS 49, 32 pp.

Sultan, E., H. Mercier, and R. Pollard, 2007: An inverse model of the large scale circulation in the south Indian Ocean. *Prog. Oceanogr.,* **74,** 71–94.

Talley, L. D., 2003: Shallow, intermediate, and deep overturning components of the global heat budget. *J. Phys. Oceanogr.,* **33,** 530–560.

——, 2008: Freshwater transport estimates and the global overturning circulation: Shallow, deep and throughflow

components. *Prog. Oceanogr.,* **78,** 257–303, doi:10.1016/j.pocean.2008.05.001.

——, J. L. Reid, and P. E. Robbins, 2003: Data-based meridional overturning streamfunctions for the global ocean. *J. Climate,* **16,** 3213–3226.

Treguier, A. M., M. H. England, S. R. Rintoul, G. Madec, J. Le Sommer, and J.-M. Molines, 2007: Southern Ocean overturning across streamlines in an eddying simulation of the Antarctic Circumpolar Current. *Ocean Sci.,* **3,** 491–507.

Weaver, A., and P. Courtier, 2001: Correlation modelling on the sphere using a generalized diffusion equation. *Quart. J. Roy. Meteor. Soc.,* **127,** 1815–1846, doi:10.1256/smsqj.57517.

Wijffels, S. E., J. M. Toole, and R. Davis, 2001: Revisiting the South Pacific subtropical circulation: A synthesis of World Ocean Circulation Experiment observations along 32°S. *J. Geophys. Res.,* **106,** 19 481–19 514.

Wunsch, C., 1998: The work done by the wind on the oceanic general circulation. *J. Phys. Oceanogr.,* **28,** 2332–2340.

——, 2010: Variability of the Indo-Pacific Ocean exchanges. *Dyn. Atmos. Oceans,* in press.

——, and P. Heimbach, 2007: Practical global oceanic state estimation. *Physica D,* **230,** 197–208, doi:10.1016/j.physd.2006.09.040.

——, and ——, 2009: The global zonally integrated ocean circulation, 1992–2006: Seasonal and decadal variability. *J. Phys. Oceanogr.,* **39,** 351–368.

Zhai, X., and R. J. Greatbatch, 2007: Wind work in a model of the northwest Atlantic Ocean. *Geophys. Res. Lett.,* **34,** L04606, doi:10.1029/2006GL028907.